CHAPTER 4

PHYSICAL AND ELECTRICAL PROPERTIES OF PZN-PZT BASED COMPOSITION

This chapter is dedicated to the investigation of physical and electrical properties of PZN-PZT based composition. There are three part, (1) synthesis, formation and characterization of PZN-PZT powders, (2) effect of PZN content on properties of PZN-PZT ceramics, and (3) effect of Zr/Ti ratio on properties of PZN-PZT ceramics. The scope of measurement is defined and the results of dielectric, piezoelectric and ferroelectric properties are presented and discussed.

4.1. Synthesis, formation and characterization of PZN-PZT powders

Lead zirconate titanate, $Pb(Zr,Ti)O_3$ or PZT, is a well known piezoelectric that has been widely employed in a large number of sensing and actuating devices. PZT ceramics have very high Curie temperature (~ 390 ^oC). They have excellent dielectric, piezoelectric and elastic properties suitable for wide range of practical applications [9, 74, 75]. Lead zinc niobate, $Pb(Zn_{1/3}Nb_{2/3})O_3$ or PZN, which exhibits a perovskite structure and a Curie temperature ~ 140 ^oC, is one of the most important relaxor ferroelectric materials with a high dielectric constant and large electrostrictive coefficient [54, 76]. These characteristics make PZN a promising candidate for high

performance electromechanical actuator and transducer applications. However, it has been recognized and widely accepted that inhomogeneous mixing in the conventional solid state reaction process leads to formation of pylochlore phase and subsequent deterioration of electrical properties in PZN ceramics [77,78]. The addition of other perovskite materials, such as barium titanate ($BaTiO_3$) [66], lead titanate ($PbTiO_3$) [65], or lead zirconate titanate (PZT) [79], has been found to be effective in stabilizing PZN in the perovskite structure. However, recent work by Fan and Kim [69] has shown promise in producing phase-pure perovskite PZN–PZT ceramics with the conventional mixed-oxide method.

The present work is aimed at synthesizing pyrochlore-free lead zinc niobate – lead zirconate titanate powders. The conventional mixed oxide synthetic route via a rapid vibro-milling has been developed with a one-step reaction of all starting materials. The rapid vibro-milling is employed for the first time in this work as a significant time-saving method to obtain single-phase PZN-PZT nano-sized powders at low temperature.

4.1.1. Experimental procedure

In this section, regent grade oxides of lead oxide, PbO (Fluka Chemical, 99.9% purity), zirconium dioxide, ZrO_2 (RdH laborchemikalin, 99.9% purity), zinc oxide, ZnO (Fluka Chemical, 99.9% purity), niobium pentaoxide, Nb_2O_5 (Aldrich, 99.9% purity), and titanium dioxide, TiO_2 (RdH laborchemikalin, 99.9% purity), were used as starting materials. PZN–PZT powders were synthesized by the solid-state reaction of these raw materials. Ground mixtures of the powders were required with

stoichiometric ratios for the general composition xPb($Zn_{1/3}Nb_{2/3}$)O_3–*(*1-*x)*Pb($Zr_{1/2}Ti_{1/2}$)O_3 where x = 0.1, 0.2, 0.3, 0.4, and 0.5. A McCrone vibro-milling technique was employed in order to combine mixing capacity with a significant time saving. The milling operation was carried out in isopropanal. High purity corundum cylindrical media were used as the milling media. After vibro-milling for 30 minutes and drying at 120°C, the reaction of the uncalcined powders taking place during heat treatment was investigated by themogravimetric and differential thermal analysis (TG-DTA, Shimadzu) in air from room temperature up to 1350°C. Based on the TG-DTA results, the mixture was calcined at temperatures between 750 to 950°C for 2 hours in alumina crucible to examine the phase formation behavior of PZN-PZT powders. A heating/cooling rate of 20°C/min was selected for all of the compositions in this system because it was shown to be effective in reducing the total amount of pyrochlore phase [80].

Calcined powders were subsequently examined by room temperature X-ray diffraction (XRD; Siemens-D500 diffractrometer) using Ni-filtered CuK_α radiation to identify the phases formed for the PZN-PZT powders. The relative amounts of perovskite and pyrochlore phases were approximated by calculating the ratio of the major XRD peak intensities of the perovskite and pyrochlore phases via the following equation [60]:

$$\text{Perovskite \%} = \left(\frac{I_{perov}}{I_{perov} + I_{pyro}} \right) \times 100 \qquad (4.1)$$

where I_{perov} and I_{pyro}, refer to the intensity of the (110) perovskite peak and (222) pyrochlore peak, respectively. Powder morphologies and particle sizes were directly

imaged using scanning electron microscopy (SEM; JEOL JSM-840A). EDX spectra were quantified with the virtual standards peaks supplied with the Oxford Instruments eXL software. Diagram of experimental procedure is shown in Fig. 4.1.

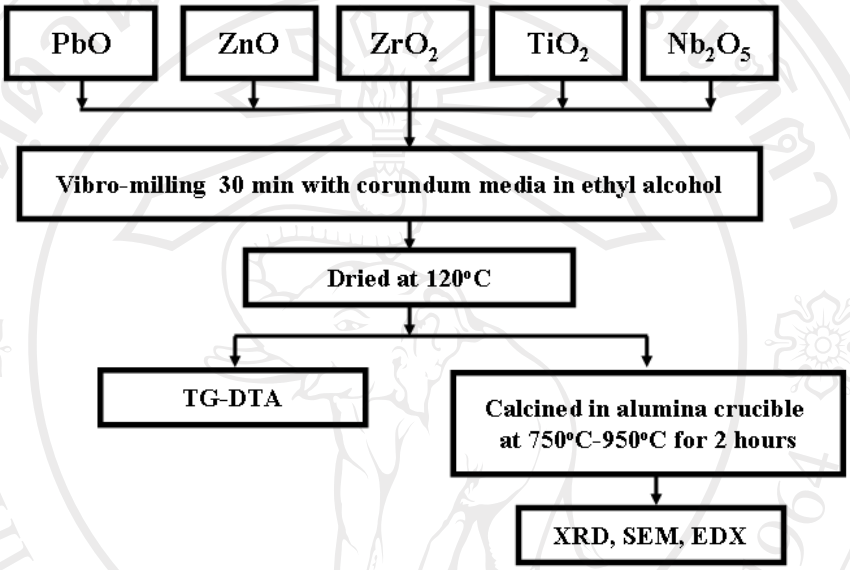

Figure 4.1 Diagram of experimental procedure.

4.1.2. Results and discussion

4.1.2.1. Themogravimetric and Differential Thermal Analysis (TG/DTA)

TG-DTA curves obtained for powders mixed in the stoichiometric proportions of PZN and PZT powders are displayed in Fig. 4.2. In the temperature range 50–200°C, the sample shows several large exothermic peaks in the DTA curve. These DTA peaks can be attributed to the decomposition of the organic species from the milling process. The different temperature, intensities, and shapes of the thermal peaks probably are related to the different natures of the organic species and, consequently, caused by the removal of species differently bounded in the network

[81]. In the temperature range 750–1050°C, both exothermic and endothermic peaks are observed in the DTA curve. The DTA curve shows that the endothermic peak centered at ~800°C may result from perovskite phase crystallization, and the last exothermic peak centered at ~ 850°C may be caused by the decomposition of lead oxide [82,83]. Above 1000°C, TG curve indicates that higher weight loss of substance occurs. This TG result implies the upper limit of the calcination temperature for the mixed powders. Therefore, these temperatures are used to define the ranges of calcination temperatures (750 to 950°C) used in subsequent powder processing steps.

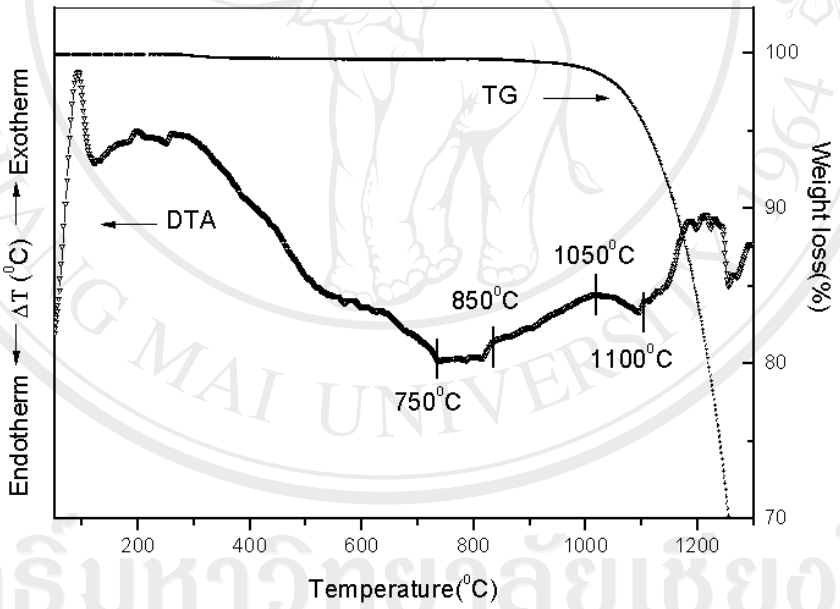

Figure 4.2 TG-DTA curves for the mixture of PbO-ZnO-Nb_2O_5-$ZrTiO_2$-TiO_2 powder.

4.1.2.2. X-Ray Diffraction Analysis (XRD)

Powder XRD patterns of the calcined 0.5PZN-0.5PZT powders at different calcination temperatures are shown in Fig. 4.3. The XRD results show that the pyrochlore phase $Pb_{1.88}(Zn_{0.3}Nb_{1.25})O_{5.305}$ (JCPDS No.25-0446) is dominant at the

calcination temperature below 850°C for the powders. The precursor phases PbO, ZnO, Nb_2O_5, ZrO_2, TiO_2 are also detected in the powders by XRD when calcined below 800°C. Other compositions also show a similar trend. The pyrochlore-free *x*PZN–(1-*x*)PZT powders with *x*= 0.1- 0.4 can be obtained at calcination temperatures above 850°C. Earlier study by Vittayakorn *et. al.* [70] also showed similar observation. However, in that study which used a convention at ball-milling method with excess PbO 2wt%, the calcination temperature was above 900°C. This clearly indicates that a rapid vibro-milling method can significantly lower the calcination temperature for PZN-PZT powders.

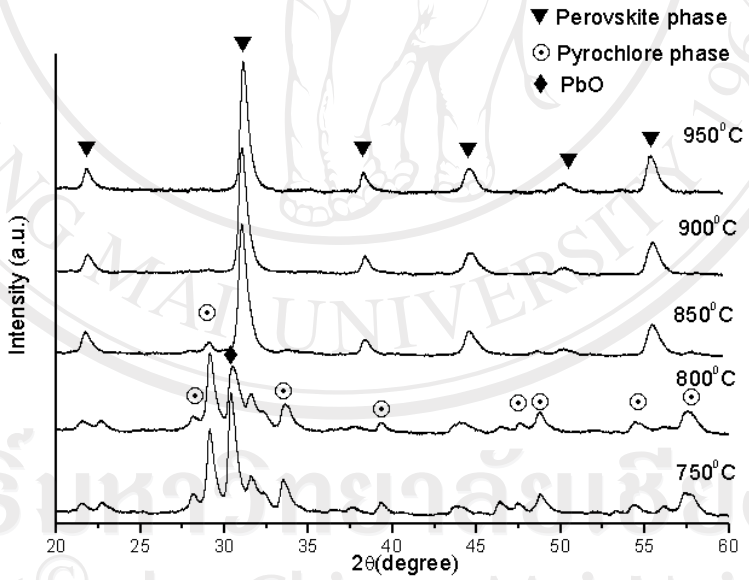

Figure 4.3 XRD patterns of 0.5PZN–0.5PZT powder calcined at various temperatures for 2 h. with heating/cooling rates of 20°C/min.

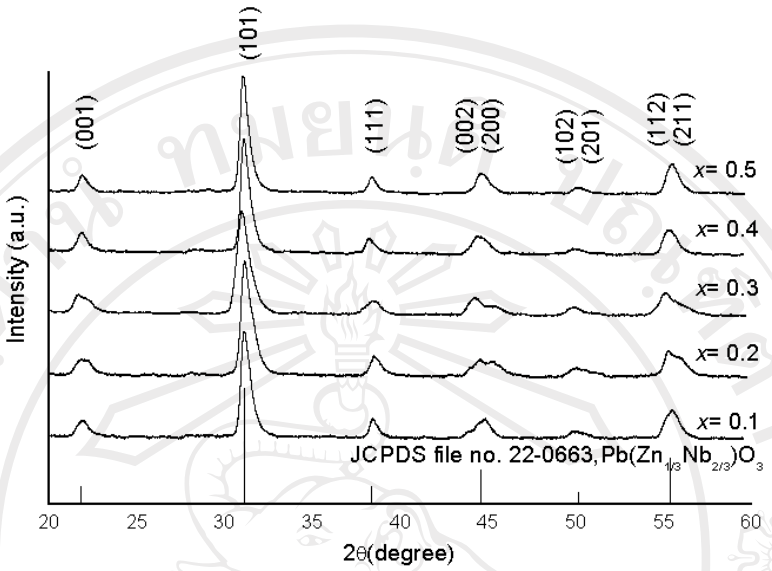

Figure 4.4 XRD patterns of the *x*PZN -(1-*x*)PZT powders (when x = 0.1, 0.2, 0.3, 0.4, and 0.5) calcined at 900°C with heating/cooling rates of 20°C/min and soaking time of 2 h.

As listed in Table 4.1, all the compositions in the present work exhibit pyrochlore-free XRD scans at calcination temperatures above 900°C. It can be noticed that in most compositions the perovskite phase is formed in a suddenly, which is significantly different from previous research [70] in which more perovskite phase was found with increasing calcination temperature. The difference could be attributed to nano-sized mixed powders obtained from a rapid vibro-milling technique. The perovskite phase formation behavior for *x*PZN–*(*1-*x)*PZT powders at the calcination temperature of 900°C is shown in Fig. 4.4. The percentage of perovskite phase in PZN-PZT powders is summarized in Table 4.1 as a function of calcination temperature. These experimental results indicate that when the concentration of the PZN phase increases the calcination temperature must be increased to obtain phase-

pure perovskite PZN-PZT powders. Even though pyrochlore-free PZN-PZT powders can be obtained at calcination temperature of 900°C for all compositions (x = 0.1-0.5), it should be noted that the on-set calcination temperature for pyrochlore-free powders starts at 800°C for composition with x = 0.1. It is also very interesting to see that these on-set temperatures in every composition are approximately 50°C lower that those reported earlier with a conventional ball-milling method [70]. More importantly, this study suggests that the conventional mixed oxide method helps to stabilize the perovskite phase and the calcination temperature can be futher reduced by a vibro-milling technique.

Table 4.1 Percentage of perovskite phase of xPZN-(1-x)PZT; x = 0.1-0.5.

Calcination Temperature(°C)	Percentage of perovskite phase				
	x = 0.1	*x = 0.2*	*x = 0.3*	*x = 0.4*	*x = 0.5*
750 °C	-	-	-	-	-
800 °C	100	78.2	-	-	-
850 °C	100	100	100	100	87.7
900 °C	100	100	100	100	100
950 °C	100	100	100	100	100

4.1.2.3. SEM and EDX analysis

The morphological changes in the PZN-PZT powders formed by a mixed oxide method are illustrated in Fig. 4.5. In general, the particles are agglomerated and basically irregular in shape, with a substantial variation in particle size, particularly in samples with more PZN contents. Generally, particle size of all compositions can be estimated from SEM micrographs to be in range of 0.2-2 μm. It should be noted that

the morphology of the calcined 0.1PZN-0.9PZT and 0.3PZN-0.7PZT powders is almost similar in size and shape, while for the other compositions the size and shape of the powders are significantly different. Finally, EDX analysis using a 20 nm probe on a large number of particles of the calcined powders confirms that the parent composition is PZN-PZT powders as shown in Fig. 4.6, in good agreement with XRD results.

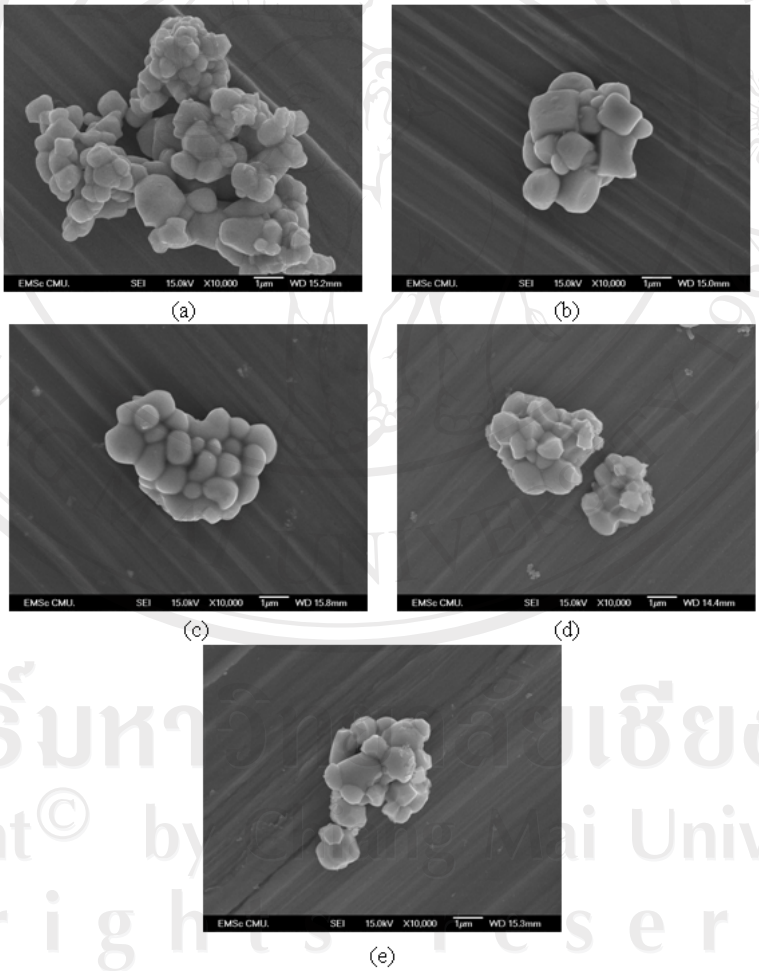

Figure 4.5 SEM micrographs of the *x*PZN-(1-*x*)PZT powders calcined at 900°C with heating/cooling rates of 20°C/min and soaking time of 2 h for (a) *x*=0.1, (b) *x*=0.2, (c) *x*=0.3, (d) *x*=0.4 and (e) *x*=0.5.

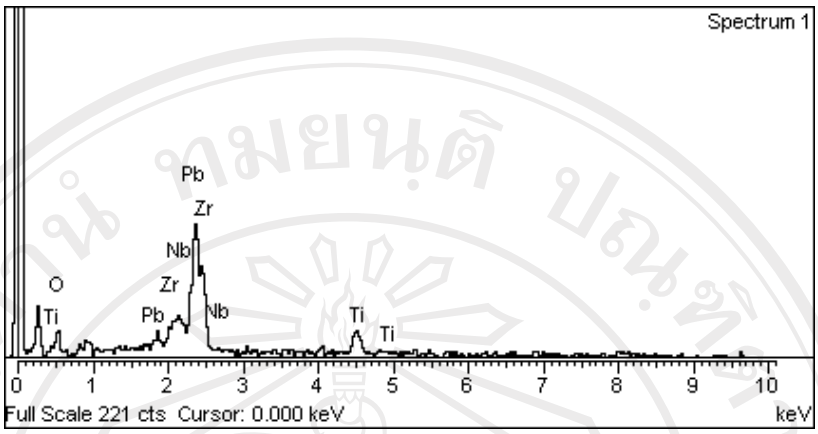

Figure 4.6 EDX analysis of the 0.2PZN-0.8PZT powders calcined at 900°C with heating/cooling rates of 20°C/min and soaking time of 2 h

4.1.3. Summary

In this study, an approach to synthesize pyrochlore-free lead zinc niobate – lead zirconate titanate powders with a formula $x\text{Pb}(\text{Zn}_{1/3}\text{Nb}_{2/3})\text{O}_3-(1-x)\text{Pb}(\text{Zr}_{1/2}\text{Ti}_{1/2})\text{O}_3$ (when x = 0.1-0.5) by a mixed oxide synthetic route via a rapid vibro-milling has been developed. The formation of perovskite phase in calcined PZN-PZT powders has been investigated as a function of calcination temperature by TG-DTA and XRD techniques. Powder morphology and chemical composition have been determined with SEM and EDX techniques. The potential of a vibro-milling technique as a significant time-saving method to obtain single-phase PZN-PZT powders at low calcination temperature is also discussed. The results indicated that at calcination condition of 900°C for 2h, with heating/cooling rates of 20°C/min single-phase PZN-PZT powders can be obtained for every composition ratio between x = 0.1-0.5.

4.2. Effect of PZN content on properties of PZN-PZT based ceramics

Recent work by Fan and Kim [69,86] has shown that the perovskite phase of $Pb(Zn_{1/3}Nb_{2/3})O_3$ (PZN) ceramics was stabilized by adding a Ti-rich side tetragonal phase of $Pb(Zr_{0.47}Ti_{0.53})O_3$ (PZT) located across the morphotropic phase boundary (MPB). When 40% PZT was added, a rhombohedral perovskite phase was formed without any trace of the pyrochlore phase. The rhombohedral phase fraction decreased markedly with increasing PZT concentration. This work has shown promise in producing pure perovskite phase PZN–PZT ceramics with the conventional mixed-oxide method making the perovskite phase structure stable and giving the significantly improved piezoelectric properties. Vittayakorn *et al.* [70, 80] has investigated processing conditions for producing phase-pure perovskite PZN–PZT ceramics with the conventional mixed-oxide method and B-site precursor. It was consistently shown that an MPB exists around $x = 0.25$ in this binary system. Excellent piezoelectric properties were found in 0.3PZN–0.7PZT, the composition closest to the MPB with a rhombohedral structure.

In previous section, we synthesized pyrochlore-free lead zinc niobate – lead zirconate titanate powders by conventional mixed oxide route via a rapid vibro-milling. A McCrone vibro-milling technique was employed in order to combine mixing capacity with significant time-saving method to obtain single-phase PZN-PZT nano-sized powders at low temperature [81]. The aim of this section was to synthesize pyrochlore-free PZN-PZT ceramics via vibro-milling methods (conventional mixed

oxide) and to investigate the dielectric, piezoelectric, and ferroelectric properties of the ceramics to identify MPB composition in this ceramic system.

4.2.1. Experimental procedure

The specimens studied were fabricated according to the formula: xPb($Zn_{1/3}Nb_{2/3}$)O_3-(1-x)Pb($Zr_{1/2}Ti_{1/2}$)O_3, where x= 0.1-0.5. Raw materials of PbO, ZrO_2, TiO_2, ZnO and Nb_2O_5 with >99% purity were used to prepare samples by a conventional mixed oxide process. The starting powders were mixied by zirconia ball media with isopropanal as a medium in a polyethylene jar for 30 min via McCrone vibro-milling technique. The mixed slurry was dried and calcined at 900^{o}C for 2h. The calcined powders were ball-milled again with additives and consolidated into disks of 12.5 mm diameter using isostatic pressing about 150 MPa. PbO-rich atmosphere sintering of the ceramics was performed in a high-purity alumina crucible at various sintering temperature between 1150 to 1250 °C depending upon the compositions, as listed in Table 4.2. The crystal structure and symmetry of the sintered bodies were examined by X-ray diffraction (XRD) and densities were measured by Archimedes method. Surface morphologies of sintered ceramics were directly imaged, using scanning electron microscopy (SEM; JEOL JSM-840A). Grain size was determined from SEM micrographs by a linear intercept method.

For electrical properties characterizations, silver electrode (Dupont, QS 171) was printed on the lapped surfaces. The electrode was fired at 850^{o}C for 45 min. The specimens were poled in silicone oil at 150^{o}C by applying a DC field of 3kV/mm for 30min. The dielectric properties of the sintered ceramics were studied as functions of

both temperature and frequency with an automated dielectric measurement system. The computer-controlled dielectric measurement system consists of a precision LCR-meter (Hewlett Packard, model 4284A), a temperature chamber, and a computer system. The capacitance and the dielectric loss tangent are determined over the temperature range of 50 and 450 °C with the frequency ranging from 100 Hz to 100 kHz. The Curie temperature (T_c) was determined by the temperature dependence of the dielectric constant at 1 kHz. The piezoelectric constant (d_{33}) was measured using a quasi-static piezoelectric d_{33} meter (Model ZJ-3d, Institute of Acoustics Academic Sinica, China). The planar coupling coefficient (k_p) and the mechanical quality factor (Q_m) were determined by the resonance and anti-resonance technique [73] using an impedance analyzer (Model HP4294A, Hewlett-Packard, CA). Ferroelectric switching measurements were made using a modified Sawyer-Tower circuit with a linear variable differential transducer (LVDT) for strain measurement, DSP lock-in amplifier (SR830, Stanford Research), high voltage power supply (TREK 609C-6, Trek), and computerized control and data acquisition. Detail of each experiment set-up have been summarized in Chapter 3.

4.2.2. Results and discussion

4.2.2.1. Crystal structure, phase formations and microstructure

Perovskite phase formation, crystal structure and lattice parameter were determined by XRD at room temperature. The XRD patterns of xPb($Zn_{1/3}Nb_{2/3}$)O_3-(1-x)Pb($Zr_{1/2}Ti_{1/2}$)O_3, where x= 0.1-0.5 are shown in Fig.4.7(a), showing perovskite structure for all compositions. The pyrochlore phase is not observed in this system.

The crystal symmetry for $Pb(Zn_{1/3}Nb_{2/3})O_3$ at room temperature is rhombohedral *R3m* with a lattice parameter a = 5.742 Å (JCPDS No. 22-0663) [88]. The crystal structure of $Pb(Zr_{1/2}Ti_{1/2})O_3$ at room temperature is tetragonal *P4mm* with a lattice parameter a = 4.031 Å and c = 4.145 Å (JCPDS No. 70-4057) [89]. Therefore, the crystal symmetry should change from tetragonal to rhombohedral due to the effects of the increased PZN fraction. In the XRD patterns, change in the crystal structure of the specimens is revealed by the (002) and (200) peaks evolving to (202) peak as shown in Figs 4.7.(a) and (b). The perovskite structure appears to change from tetragonal to rhombohedral across the MPB with the increasing amount of PZN content around 20-30 mol%. As shown in Fig. 4.7(b), XRD peak profiles of the (200) and (002) peaks at x = 0.1 indicate a tetragonal phase. At the x = 0.2–0.3 compositions, (202) peak is observed, indicating the co-existence of the rhombohedral and tetragonal phases. The (202) peak in compositions x = 0.4 and 0.5 is clearly observed, indicating that the crystal transformed into rhombohedral phase. Previously, Vittayakorn *et al.* [80] has investigated processing conditions for producing phase-pure perovskite PZN–PZT ceramics with the conventional mixed-oxide method and B-site precursor. This earlier work consistently showed that an MPB existed around x = 0.25 in this binary system, which is in good agreement with this current study.

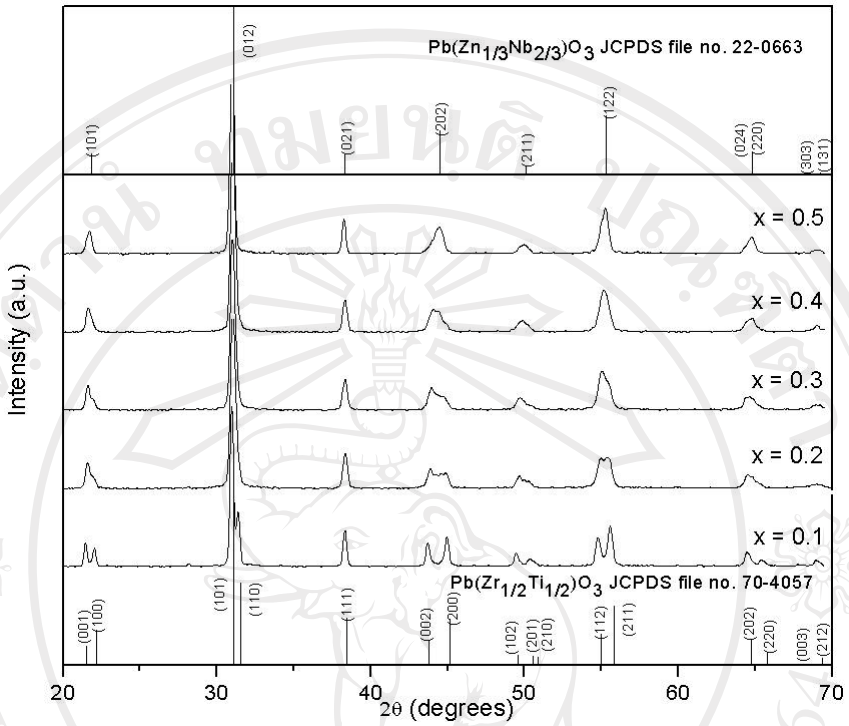

(a)

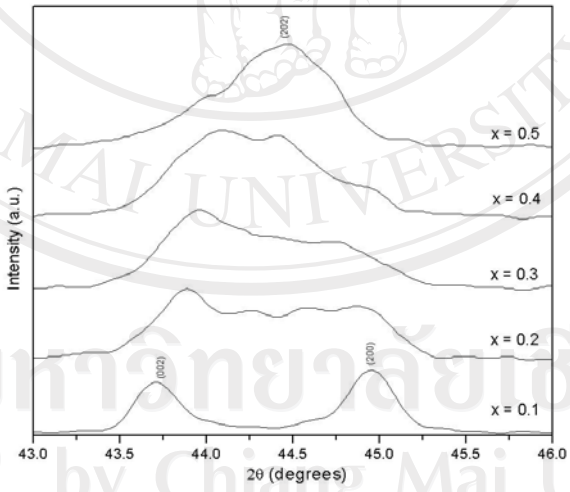

(b)

Figure 4.7 (a)XRD diffraction patterns of sintered *x*PZN-(1 − *x*)PZT ceramics. (b) selected region of the diffraction patterns.

Figure 4.8 shows SEM photographs of the surfaces of xPb($Zn_{1/3}Nb_{2/3}$)O_3-(1-x)Pb($Zr_{1/2}Ti_{1/2}$)O_3 ceramics, where x= 0.1-0.5. As shown in Figs. 4.8(a-c), the grain sizes of the ceramics are decreased with increasing amount of PZN content up to x = 0.3. However, the SEM micrographs in Fig. 4.8(d-e) show that increasing grain size is observed when the amount of PZN is increased further. The micrographs also show that the grain size of the ceramics ranges from 0.5 to 5 μm, as listed in Table 4.2. The average grain size decreased significantly from 4.2 μm in 0.1PZN-0.9PZT to about 1.5 to 2 μm in other compositions. Along with the average grain size, the density of specimen was changed by the addition of PZN, as also observed in earlier work [86]. With increasing PZN content in the specimen, the grain size apparently decreased. The density and the average grain size of the specimen (as a function of PZN content) are list in Table 4.2.

Table 4.2 Physical properties of xPZN–(1 − x)PZT ceramics

x	Sintering temp (^oC)	Density (g/cm^3)	Grain size range(μm)	Average grain size (μm)
0.1	1225	7.713	1.5 - 5.0	4.223
0.2	1200	7.826	0.5 - 2.0	1.726
0.3	1175	7.873	0.5 – 1.5	1.487
0.4	1150	7.951	1.0 - 2.0	1.718
0.5	1150	7.977	1.0 - 2.5	2.058

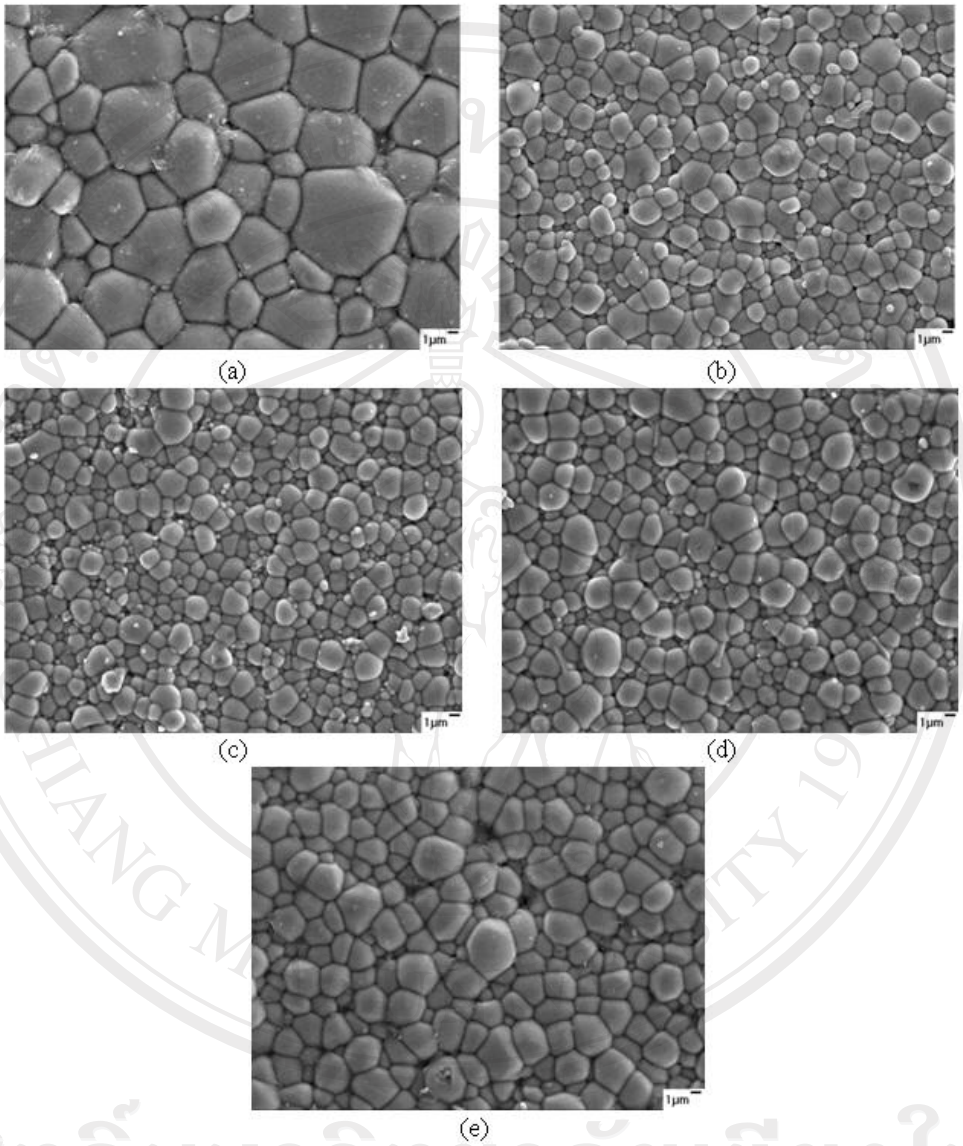

Figure 4.8 SEM micrographs of *x*PZN-(1−*x*)PZT ceramics with various compositions: (a) $x = 0.1$, (b) $x = 0.2$, (c) $x = 0.3$, (d) $x = 0.4$, and (e) $x = 0.5$.

4.2.2.2. Dielectric properties

The temperature and frequency dependence of the dielectric constant (ε_r) and dielectric loss tangent (tan δ) for *x*PZN–(*1*-*x*)PZT, $x = 0.1$ - 0.5 is shown in Fig. 4.9. The maximum dielectric constant at 1 kHz (ε_m @ 1 kHz) is listed in Table 4.3. For

better comparison, the temperature dependence of dielectric constant (ε_r) and dielectric loss tangent (tan δ) at 1 kHz is plotted in Fig. 4.10. A clear transition in T_m (defined as the temperature at which ε_r is maximum at 1 kHz) is observed. It is seen that an increase in PZN mole fraction leads to a decrease in T_m.

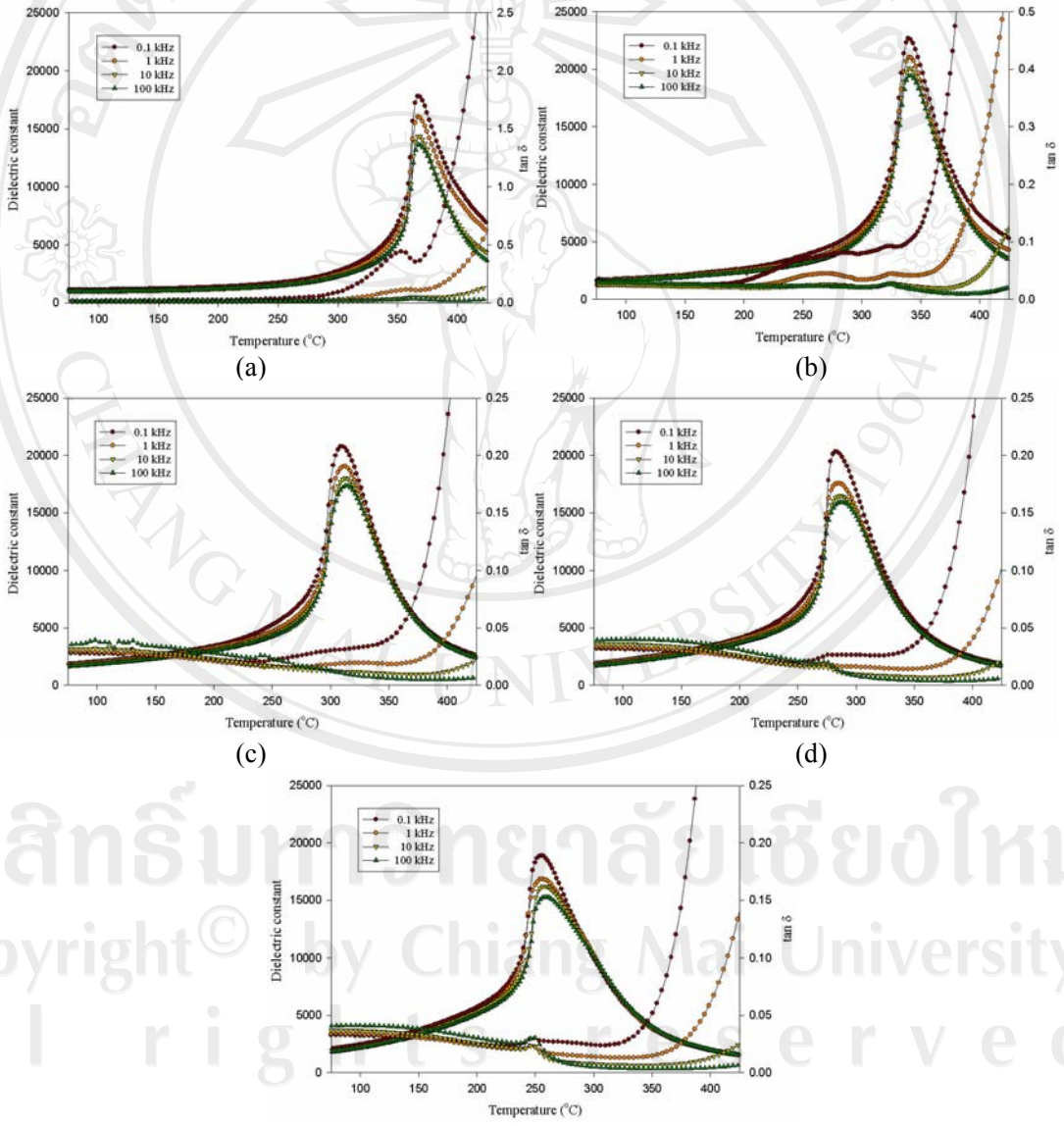

Figure 4.9 Temperature and frequency dependence of dielectric properties of *x*PZN-(1 − *x*)PZT ceramics ;(a) *x* = 0.1, (b) *x* = 0.2, (c) *x* = 0.3, (d) *x* = 0.4, and (e) *x* = 0.5.

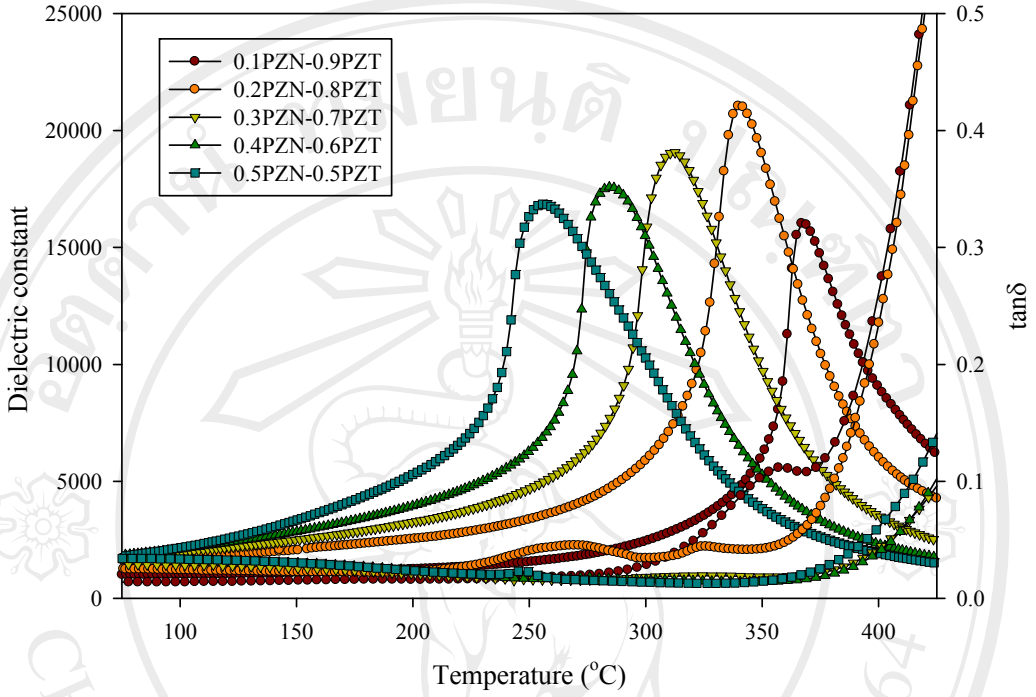

Figure 4.10 Temperature dependence of dielectric properties of *x*PZN-(1−*x*)PZT ceramics at 1kHz.

The maximum dielectric constant ε_{max} and T_m as a function of the mole fraction of PZN are reported in Fig 4.11 and Table 4.3. There is a good linear relationship between T_m and x, indicating that this system is a well-behaved complete solid solution. The T_m of the constituent compounds PZN and PZT are 140°C [53] and 392.6°C [90], respectively, which can be used to calculate an empirical estimate of T_m via the equation:

$$T_m = x(140^oC) + (1-x)(392.6^oC) \quad (4.2)$$

The variation of the measured T and the calculated T_m, ε_{max} as a function of composition x is shown in Fig 4.11. It is evident that Eq. (4.2) gives a reasonable approximation of the transition temperature T_m. This result suggests that the

transition temperature of xPZN-(1 − x)PZT system can be varied over a wide range from 250 to 370°C by controlling the amount of PZN content in the system. It should be noticed from the temperature and frequency dependence of the dielectric properties that PZN-PZT ceramics obtained in this study exhibit dominantly on a normal ferroelectric behavior, indicated by rather sharp phase-transformation with relatively frequency-independent dielectric properties (except in the vicinity of the transition temperature) [91]. However, with increasing PZN content a broader phase–transitions behavior is observed.

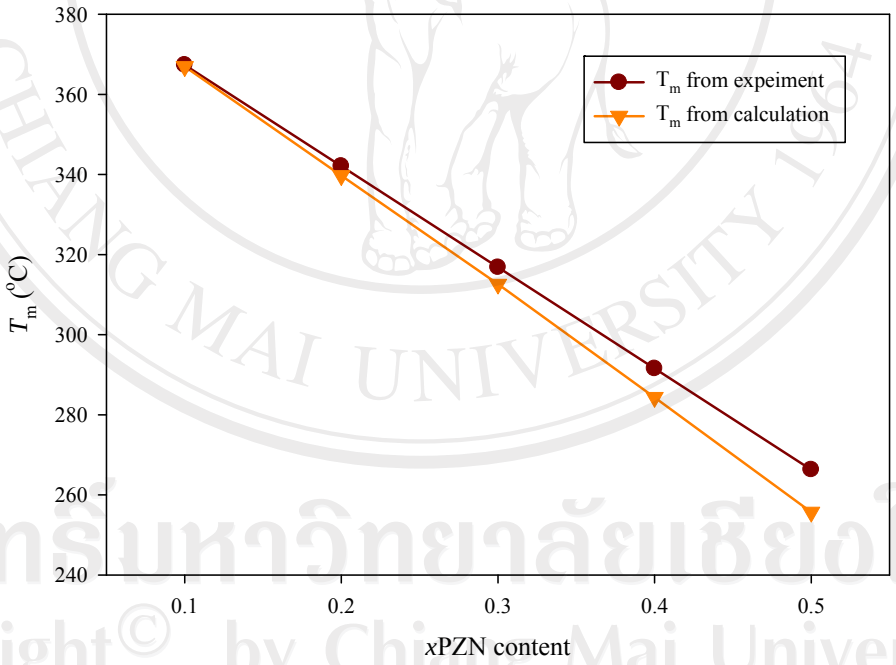

Figure 4.11 T_m calculated and T_m from maximum ε_r as a function of composition x at1 kHz.

It is well known that the permittivity of a first-order normal ferroelectric can be described by the Curie-Weiss law and a second-order relaxor ferroelectric can be described by a simple quadratic law [92]. This arises from the fact that the total

number of relaxors contributing to the permittivity response in the vicinity of the permittivity peak is temperature dependent, and the temperature distribution of this number is given by a Gaussian function about a mean value T_o with a standard deviation δ. The relative permittivity can be derived via using the equation

$$\frac{\varepsilon_m}{\varepsilon(f,T)} = 1 + \frac{(T - T_m(f))^\gamma}{2\delta^2} \tag{4.3}$$

where ε_m is the maximum value of the permittivity at $T=T_m(f)$. The value of γ is the expression of the degree of dielectric relaxation in the relaxor ferroelectric material. When γ = 1 Eq. (4.3) expresses Curie-Weiss behavior, while for γ = 2 this equation is identical to the quadratic relationship. The parameter δ can be used to measure the degree of diffuseness of the phase transition in mixed relaxor-normal ferroelectric materials.

Plots of $\log[(\varepsilon_m/\varepsilon)-1]$ vs. $\log(T-T_m)$ for x = 0.1 to 0.5 are shown in Fig. 4.12, where linear relationships can be clearly seen. The γ and δ values of compositions in the system are represented in Fig. 4.13. The parameter γ is determined from a slope of the plots to be between 1.34 and 1.95 and the diffusiveness parameter δ is the intercept values ranging between 9.9 and 35.9 as shown in Table 4.3. As the PZN mole fraction increases, the solid solution displays more relaxor-like characteristics with diffused phase transition behavior. It was reported earlier that the xPZN–(1-x)PZT systems showed strong relaxor behavior phase when x > 0.5 [70].

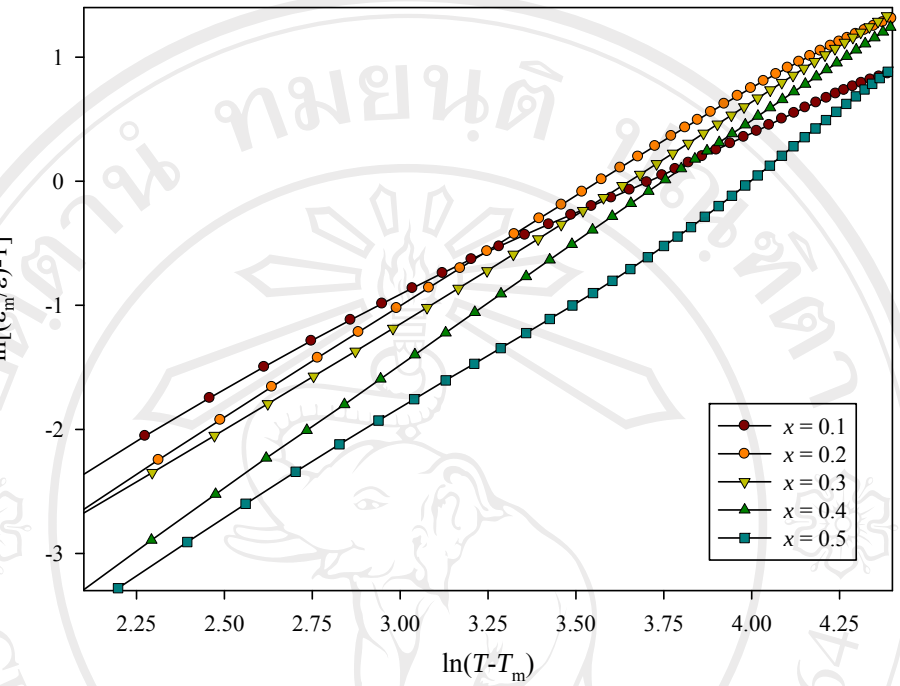

Figure 4.12 Dependence of log $[(\varepsilon_m/\varepsilon)-1]$ with $\log(T-T_m)$ for xPZN-(1−x)PZT ceramics.

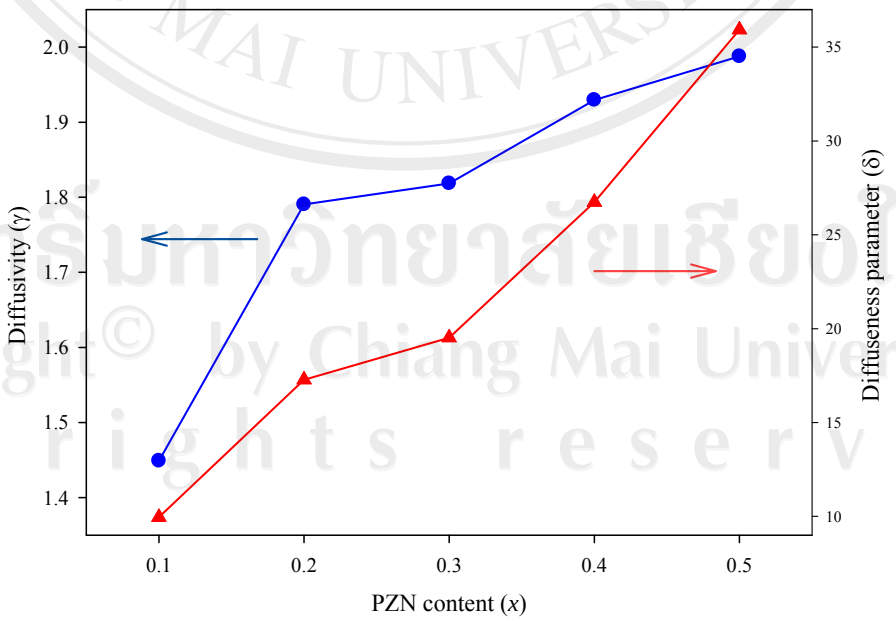

Figure 4.13 Dependence of diffusivity (γ) and diffuseness parameter (δ) for xPZN-(1−x)PZT ceramics.

Table 4.3 Dielectric properties of *x*PZN–(1−*x*)PZT ceramics

x	T_c (°C)	Dielectric properties (at 25 °C, 1 kHz)		Dielectric properties (at T_m)		Diffusivity (γ) (at 1 kHz)	Diffuseness parameter (δ) (at 1 kHz)
		ε_r	tanδ	ε_r	tanδ		
0.1	366.9	996	0.0169	16028	0.1196	1.449	9.959
0.2	339.7	1575	0.0249	21047	0.0420	1.790	17.275
0.3	312.6	1625	0.0278	19060	0.0193	1.819	19.523
0.4	284.3	1616	0.0325	17580	0.0164	1.929	26.742
0.5	255.7	1566	0.0355	16854	0.0194	1.987	35.921

4.2.2.3. Piezoelectric properties

Density, dielectric constant (ε_r), electromechanical coupling factor (k_p), mechanical quality factor (Q_m) and piezoelectric constant (d_{33}) are plotted as a function of the amount of PZN content in Fig 4.14. The density is increased with increase of PZN contents approximately from 7.7 to 7.9 g/cm^3. Moreover, the variation of piezoelectric and dielectric properties shows similar trend to that of density as shown in Table 4.4. Therefore, the improved piezoelectric and dielectric properties, might be due to the increased density. In addition, this softening effect is confirmed by the increasing of ε_r , k_p and d_{33} value, which were of the order of those reported earlier [69], and the decrease of Q_m, as shown in Fig 4.14.

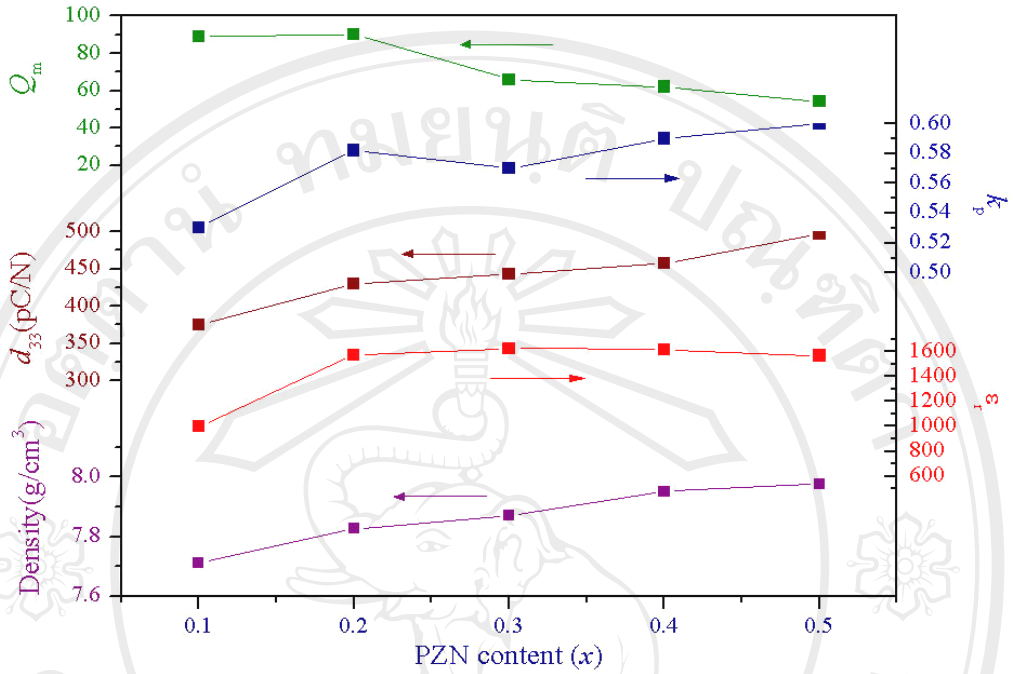

Figure 4.14 Density, dielectric constant (ε_r), piezoelectric constant (d_{33}), electromechanical coupling factor (k_p), and mechanical quality factor (Q_m) of xPZN-(1−x)PZT ceramics.

Table 4.4 Piezoelectric, ferroelectric and strain properties of xPZN-(1−x)PZT ceramics

x	Piezoelectric properties			Ferroelectric properties (at 25 °C)						Strain % @ 4MV/m
	d_{33} (pC/N)	k_p	Q_m	P_r (C/m^2)	P_s (C/m^2)	E_C (MV/m)	P_r/P_s	E_c/E_{max}	Loop squareness (R_{sq})	
0.1	375	0.53	89	0.196	0.211	2.35	0.929	0.575	1.483	0.189
0.2	430	0.58	90	0.287	0.300	1.97	0.957	0.482	1.607	0.278
0.3	443	0.57	66	0.321	0.337	1.31	0.953	0.320	1.648	0.397
0.4	457	0.59	62	0.375	0.393	1.19	0.954	0.291	1.719	0.432
0.5	497	0.60	54	0.403	0.420	0.99	0.960	0.242	1.736	0.508

4.2.2.4. Ferroelectric properties

The polarization-field (P–E) hysteresis loops of xPZN–$(1-x)$PZT ceramics are displayed in Fig. 4.15. The well-developed and fairly symmetric hysteresis loops with the field are observed for all compositions. To further assess ferroelectric characteristics in PZN-modified PZT ceramics, the ferroelectric parameters, i.e. the remnant polarization (P_r) and the coercive field (E_c), have been extracted from the experimental data, as given in Table 4.4. However, since the ferroelectric properties of the ceramics depend strongly on both the poling and measuring fields, the ferroelectric parameters have been normalized in forms of P_r/P_s and E_c/E_{max} values, where P_s is the saturated polarization, E_{max} is maximum applied field. These normalized values are also listed in Table 4.4. It can be seen clearly that P_r/P_{max} increases with an addition of PZN into the PZN–PZT composition and reachs the maximum values at 0.5PZN–0.5PZT composition, where P_r achieves the level of 96% of the maximum polarization and E_c is as small as 24.2% of the maximum applied field. The ferroelectric characteristics can also be assessed with the hysteresis loop squareness (R_{sq}), which can be calculated from the empirical expression $R_{sq}=(P_r/P_s)+(P_{1.1Ec}/P_r)$, where P_r is the remnant polarization, P_s is the saturated polarization obtained at some finite field strength below the dielectric breakdown and $P_{1.1Ec}$ is the polarization at the field equal to $1.1E_c$ [93]. For the ideal square loop, R_{sq} is equal to 2.00. As listed in Table 4.4, the loop squareness parameter R_{sq} increases from 1.483 in 0.1PZN–0.9PZT to reach the maximum value of 1.736 in 0.5PZN–0.5PZT. This can be attributed to the increase transformation of rhombohedral

domains into tetragonal domains as the tetragonal symmetry in the PZT system decreases with the increase in PZN content [9, 70, 74].

The longitudinal strain (*s*) of the specimens as a function of the electric field is shown in Fig. 4.16. The strains are enhanced markedly when PZN content is increased. This trend matched well with d_{33} and k_p as shown in Fig. 4.14. The strain level is strongly dependent on the PZN content which controlled by rhombohedral domains. When PZN content increases, the highest strain (0.508% at 4 MV/m) is observed when x= 0.5, as listed in Table 4.4.

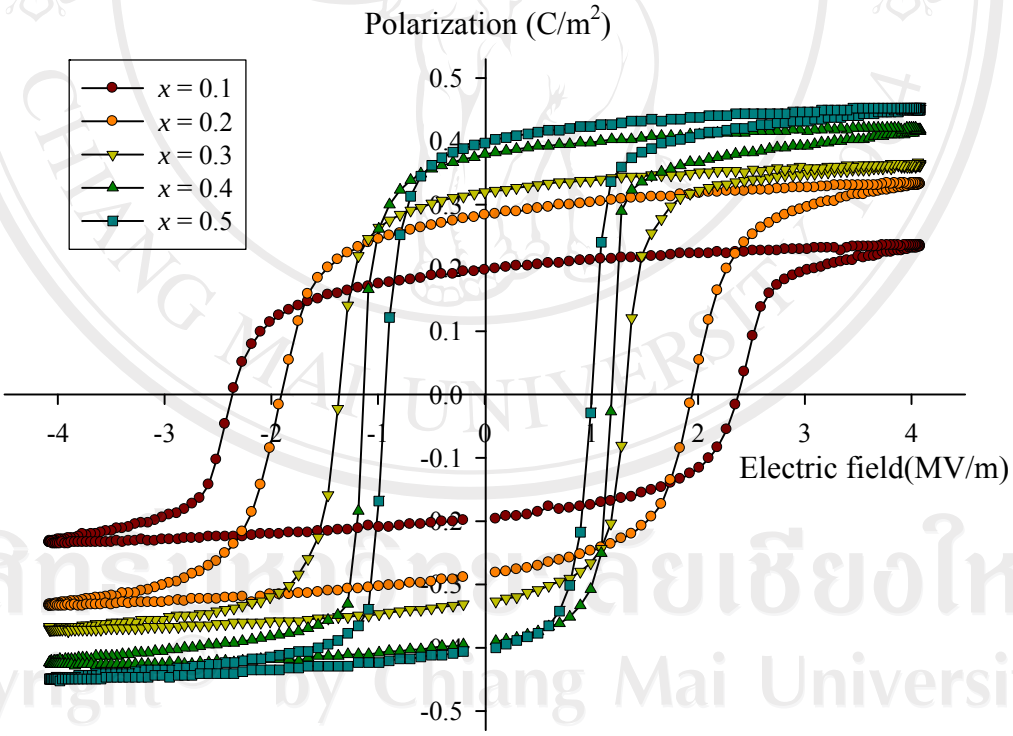

Figure 4.15 Polarization and electric filed of *x*PZN–(1−*x*)PZT ceramics with x = 0.1- 0.5.

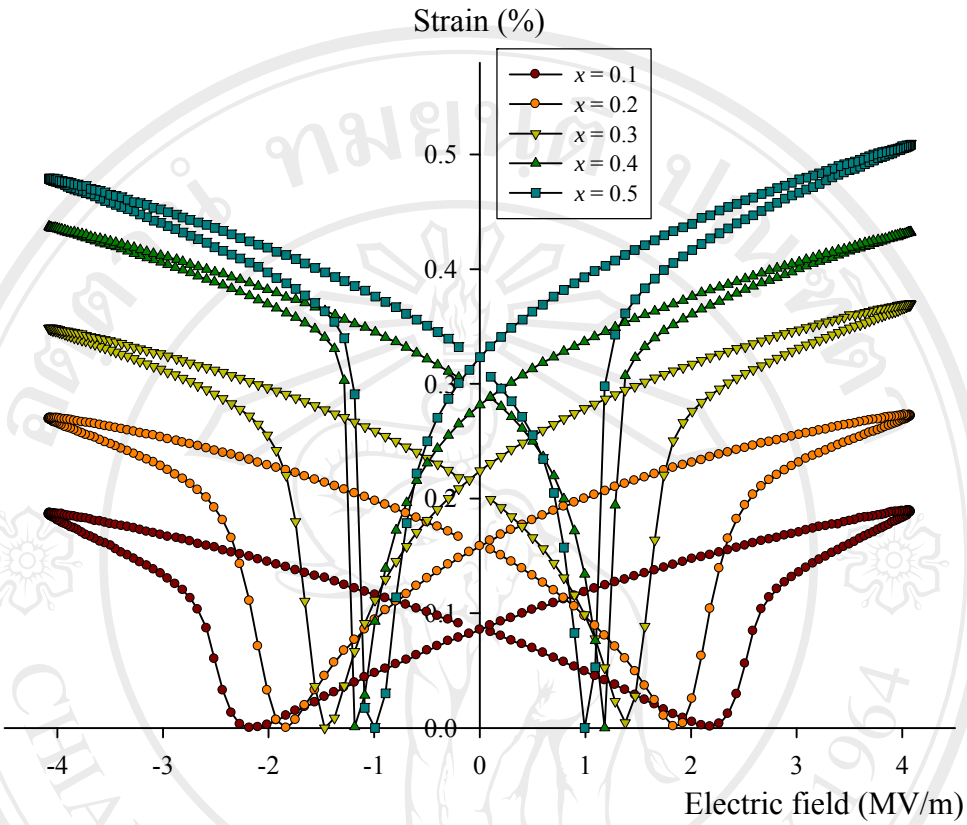

Figure 4.16 Strain and electric filed of *x*PZN–(1−*x*)PZT ceramics with *x* = 0.1- 0.5.

With addition of PZN, a structure symmetry changes from the tetragonal to rhombohedral in the composition range of *x*=0.2-0.3 for *x*PZN–(1-*x*)PZT system. Therefore, this composition corresponds to the MPB as indicated by softening behavior in PZT ceramics which confirmed by the improved electrical properties such as increasing of ε_r , k_p and d_{33} and reduced sintering temperature of PZT ceramics with increasing PZN content [86].

4.2.3. Summary

Ceramics in the xPb($Zn_{1/3}Nb_{2/3}$)O_3–(1-x)Pb($Zr_{1/2}Ti_{1/2}$)O_3 [xPZN–(1-x)PZT] solid solution system are expected to display excellent dielectric, piezoelectric, and ferroelectric properties in compositions close to the morphotropic phase boundary (MPB). The electrical behavior of the ceramics with x = 0.1 – 0.5 has been characterized in order to identify the MPB compositions in this system with combination of x-ray diffraction analysis, dielectric, piezoelectric and ferroelectric measurements, it was consistently shown that an MPB between tetragonal and rhombohedral phase exists around x = 0.2-0.3 in this binary system. In addition, the transition temperature decreased with increasing PZN content in the system. The variation of piezoelectric and dielectric properties showed increasing similar trend to density. The *P–E* and *s-E* loops demonstrated that PZN–PZT system changed gradually from tetragonal phase to the rhombohedral phase. These results clearly showed the significance of PZN in controlling the electrical responses of the PZN–PZT system.

4.3. Effect of Zr/Ti ratio on properties of PZN-PZT based ceramics

Eariler, Vittayakorn *et al.*[70, 80] has shown that excellent piezoelectric properties of PZN-PZT system were found in 0.2PZN–0.8PZT composition, which is closest to the MPB with a co-existence of the rhombohedral and tetragonal phase. Jiang *et al.* [94] studied the influence of $PbZrO_3/PbTiO_3$ ratio on diffuse phase transition of Pb($Zn_{1/3}Nb_{2/3}$)O_3– $PbZrO_3$-$PbTiO_3$ system near the morphotropic phase boundary. It is found that the extent of diffuse phase transition of PZN–PZ–PT

increased with the increase of $PbZrO_3/PbTiO_3$ ratio. The aim of this section is to study the influence of Zr/Ti ratio on the properties $0.2Pb(Zn_{1/3}Nb_{2/3})O_3$-$0.8Pb(Zr_xTi_{1-x})O_3$ ceramics, and to correlate the presence of pure perovskite phases with the optimal dielectric, piezoelectric, and ferroelectric properties on PZN-based ceramics.

4.3.1. Experimental procedure

The specimens studied were fabricated according to the formula: $0.2Pb(Zn_{1/3}Nb_{2/3})O_3$-$0.8Pb(Zr_xTi_{1-x})O_3$, where x= 0.40, 0.45, 0.50, 0.52, 0.55 and 0.60. Raw materials of PbO, ZrO_2, TiO_2, ZnO and Nb_2O_5 with >99% purity were used to prepare samples by a conventional mixed oxide process. The starting powders were mixied by zirconia ball media with isopropanal as a medium in a polyethylene jar for 30 min via vibro-milling technique. The mixed slurry was dried and calcined at 900^{o}C for 2h. The calcined powders were ball-milled again with additives and consolidated into disks of 12.5 mm diameter using isostatic pressing about 150 MPa. PbO-rich atmosphere sintering of the ceramics was performed in a high-purity alumina crucible at 1200 °C for 2h. The crystal structure and symmetry of the sintered bodies were examined by X-ray diffraction (XRD) and densities were measured by Archimedes method. Surface morphologies of sintered ceramics were directly imaged, using scanning electron microscopy (SEM; JEOL JSM-840A). Grain size was determined from SEM micrographs by a linear intercept method as described in Chapter 3 and previous sections. Electrical characterizations were also carried out with similar procedure as described in section 4.2.1.

4.3.2. Results and discussion

4.3.2.1. Crystal structure, phase formations and microstructure

Perovskite phase formation, crystal structure and lattice parameters were determined by XRD at room temperature. The XRD patterns of $0.2Pb(Zn_{1/3}Nb_{2/3})O_3$-$0.8Pb(Zr_xTi_{1-x})O_3$, where x= 0.40, 0.45, 0.50, 0.52, 0.55 and 0.60 are shown in Fig.4.17(a), showing perovskite structure for all compositions. The pyrochlore phase is not observed in this system. In the XRD patterns, the crystal structure of the specimens appears clearly to change from tetragonal to rhombohedral in all peaks due to the increase of Zr contents, as shown in Figs 4.17.(a). It is noticed that an MPB should exist around Zr/Ti = 50/50. As shown in Fig. 4.16(b), XRD peak profiles of the (200) and (002) peaks at x = 0.40, 0.45 indicate tetragonal phase. At the x = 0.50 and 0.52 compositions, (202) peak is observed, indicating the co-existence of the rhombohedral and tetragonal phase. The (202) peak in compositions x = 0.55 and 0.60 is clearly observed, indicating that the crystal transformed into rhombohedral phase. This behavior is similar to that observed with increasing PZN content in PZT based ceramics, as reported earlier [70].

Figure 4.18 shows SEM photographs of the surfaces of $0.2Pb(Zn_{1/3}Nb_{2/3})O_3$-$0.8Pb(Zr_xTi_{1-x})O_3$, where x= 0.40, 0.45, 0.50, 0.52, 0.55 and 0.60. As shown in Fig. 4.18(a-b), the microstructures of Zr/Ti = 40/60 and 45/50 show evidence of liquid phase sintering. This is probably due to both compositions have rich-$PbTiO_3$ that helps to reduce sintering temperature of system [95]. However, the SEM micrographs in Fig. 4.18(c-f) show that the grain sizes of the ceramics are slightly increased with

increased amount of Zr content. In addition, the micrographs show that the grain size of the ceramics ranges from 0.5 to 2.5 μm, as also listed in Table 4.5.

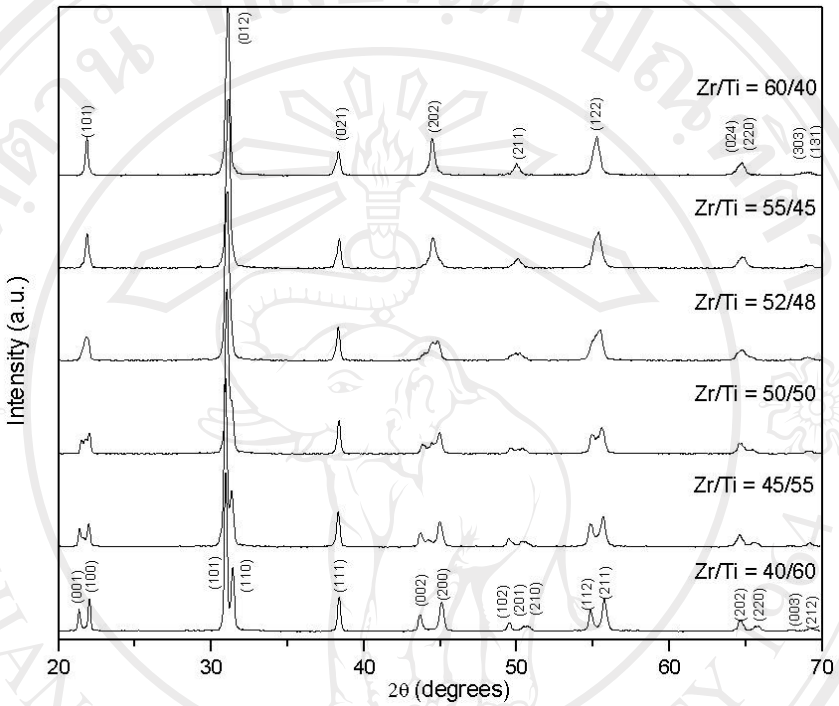

Figure 4.17 (a) XRD diffraction patterns of sintered $0.2Pb(Zn_{1/3}Nb_{2/3})O_3$-$0.8Pb(Zr_xTi_{1-x})O_3$ ceramics. (b) selected region of the diffraction patterns.

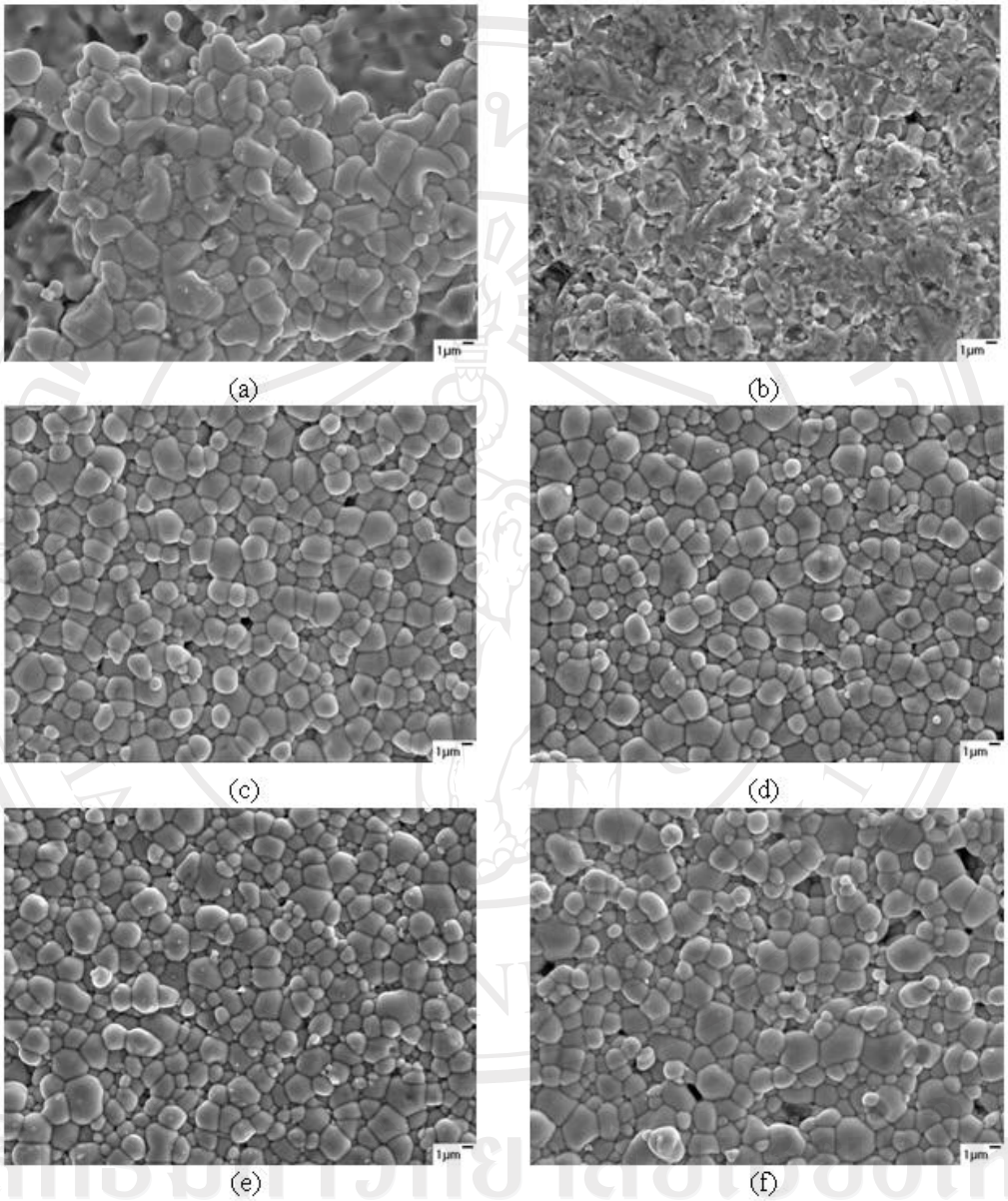

Figure 4.18 SEM micrographs $0.2Pb(Zn_{1/3}Nb_{2/3})O_3$-$0.8Pb(Zr_xTi_{1-x})O_3$ ceramics with various compositions: (a) $x = 0.40$, (b) $x = 0.45$, (c) $x = 0.50$, (d) $x = 0.52$, (e) $x = 0.55$, and (f) $x = 0.60$.

Table 4.5 Physical properties of $0.2Pb(Zn_{1/3}Nb_{2/3})O_3$-$0.8Pb(Zr_xTi_{1-x})O_3$ ceramics

Zr/Ti ratio	Density (g/cm^3)	Grain size range(μm)	Average grain size (μm)
40/60	7.957	-	-
45/55	7.888	-	-
50/50	7.826	0.5 - 2.0	1.726
52/48	7.804	0.5 - 2.0	1.765
55/45	7.745	0.5 - 2.0	1.771
60/40	7.679	1.0 - 2.5	2.082

4.3.2.2. Dielectric properties

The temperature and frequency dependence of the dielectric constant (ε_r) and dielectric loss tangent (tan δ) of $0.2Pb(Zn_{1/3}Nb_{2/3})O_3$-$0.8Pb(Zr_xTi_{1-x})O_3$ ceramics, where x= 0.40, 0.45, 0.50, 0.52, 0.55 and 0.60 are shown in Fig. 4.19. The maximum dielectric constant at 1 kHz (ε_m @ 1 kHz) is listed in Table 4.6. For better comparison, the temperature dependence of dielectric constant (ε_r) and dielectric loss tangent (tan δ) at 1 kHz is plotted in Fig. 4.20. A clear transition in T_m (defined as the temperature at which ε_r is maximum at 1 kHz) is observed. As shown in Figs. 4.19(a-f), it is found that ε_{max} increases with Zr content probably due to the presence of more rhombohedral phase [3]. It is also shown that an increase in Zr mole fraction leads to a decrease in T_m as clearly seen in Fig. 4.20.

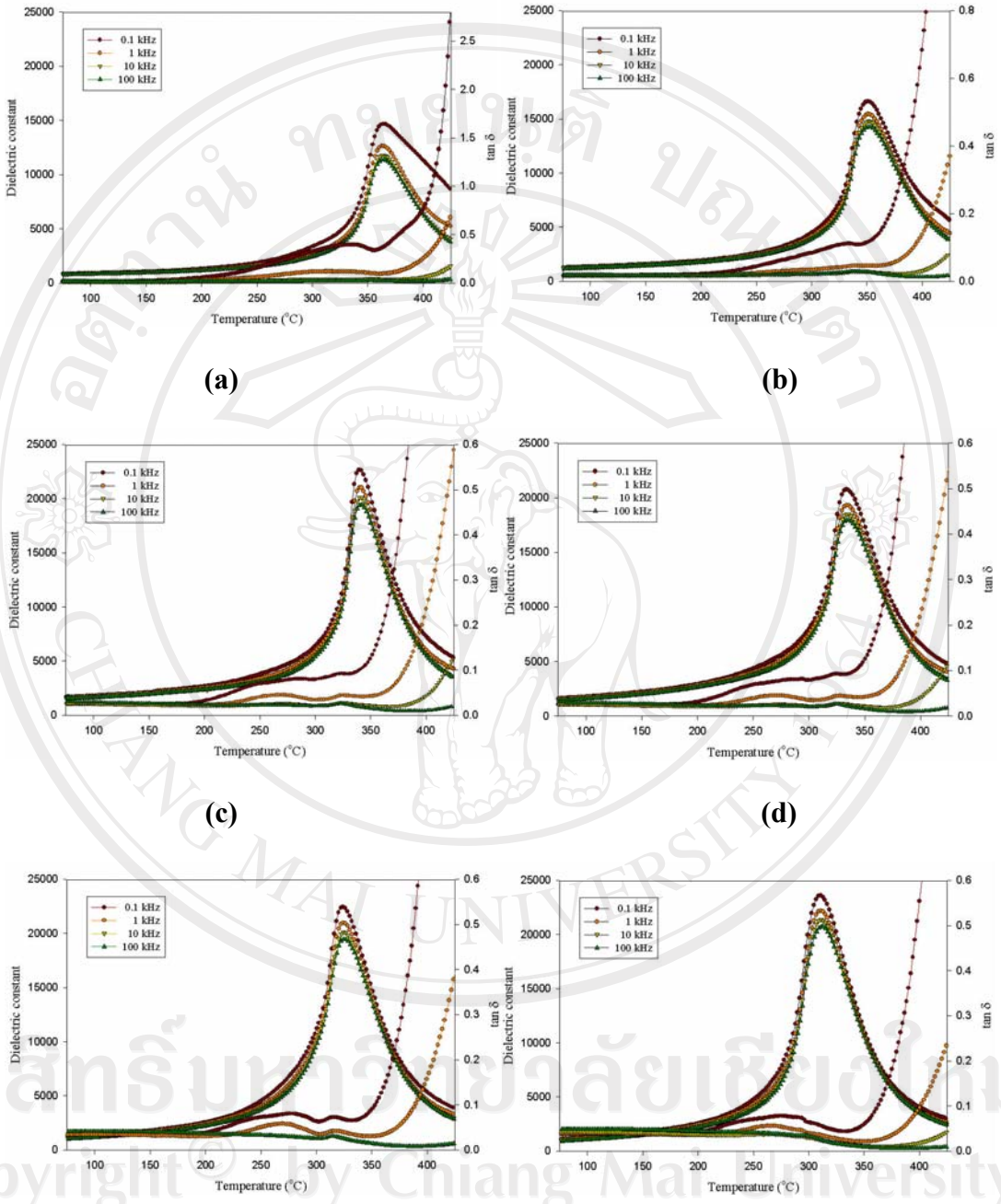

Figure 4.19 Temperature and frequency dependence of dielectric properties of $0.2Pb(Zn_{1/3}Nb_{2/3})O_3$-$0.8Pb(Zr_xTi_{1-x})O_3$ ceramics; (a) $x = 0.40$, (b) $x = 0.45$, (c) $x = 0.50$, (d) $x = 0.52$, (e) $x = 0.55$, and (f) $x = 0.60$.

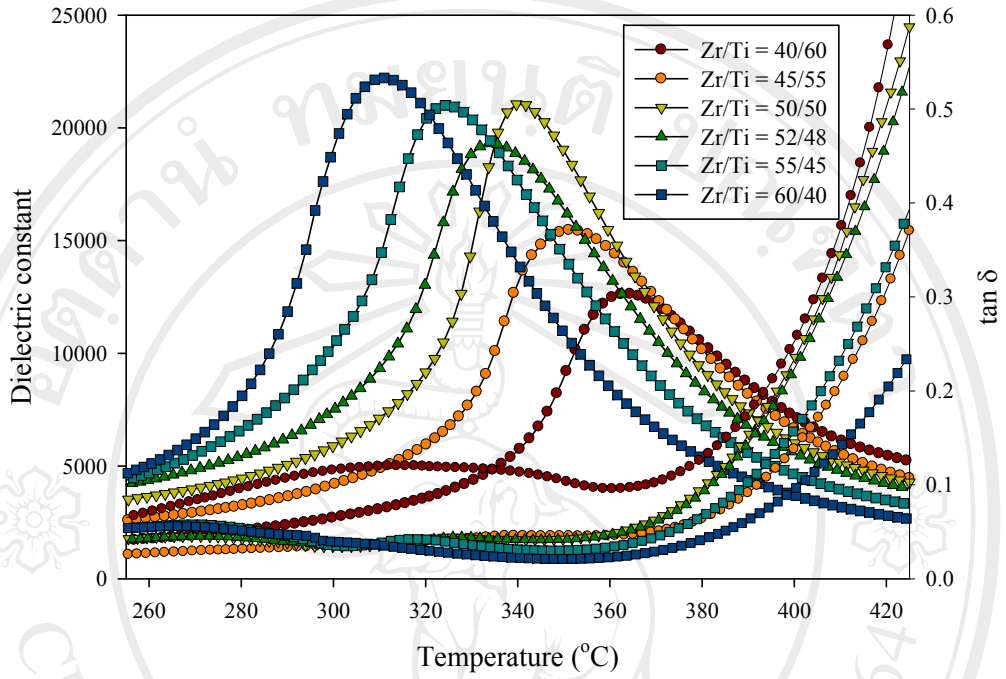

Figure 4.20 Temperature dependence of dielectric properties of $0.2Pb(Zn_{1/3}Nb_{2/3})O_3$-$0.8Pb(Zr_xTi_{1-x})O_3$ ceramics at 1kHz.

The maximum dielectric constant ε_{max} and T_m as a function of the mole fraction of Zr are represented in Fig 4.21 and Table 4.6. There is a good linear relationship between T_m and x, indicating that this system is a well-behaved complete solid solution. The T_m of the constituent compounds PZN and PZT (depend on Zr/Ti ratio) are 140°C [53] and 360-420°C [26], respectively, which can be used to calculate an empirical estimate of T_m via the equation:

$$T_m = x(140^oC) + (1-x)T_{Zr/Ti} \quad (4.4)$$

The variation of the measured T and the calculated T_m, ε_{max} as a function of composition x is shown in Fig 4.21. It is evident that Eq. (4.4) gives a reasonable approximation of the transition temperature T_m. This result suggests that the

transition temperature of xPZN-(1 − x)PZT system can be varied over a wide range from 310 to 370°C by controlling the Zr/Ti ratio in the system. It should be noticed from the temperature and frequency dependence of the dielectric properties that PZN-PZT ceramics obtained in this study exhibit a normal ferroelectric behavior, indicated by rather sharp phase-transformation with relatively frequency-independent dielectric properties (expcept in the vicnity of the transition temperature) [91]. However, with increasing Zr content a slightly broader phase transitions is observed behavior [86].

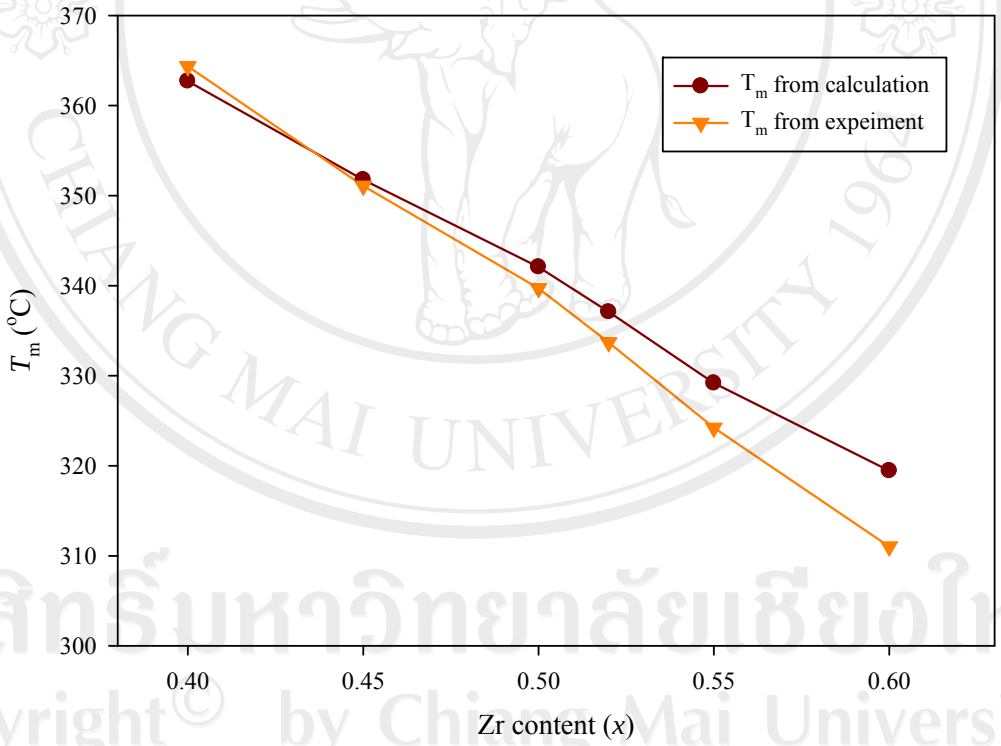

Figure 4.21 T_m calculated and T_m from maximum ε_r as a function of composition x at 1 kHz.

Table 4.6 Dielectric properties of $0.2Pb(Zn_{1/3}Nb_{2/3})O_3$-$0.8Pb(Zr_xTi_{1-x})O_3$ ceramics

Zr/Ti ratio	T_c (°C)	Dielectric properties (at 25 °C, 1 kHz)		Dielectric properties (at T_m)		Diffusivity (γ) (at 1 kHz)	Diffuseness parameter (δ) (at 1 kHz)
		ε_r	tan δ	ε_r	tan δ		
40/60	364.4	996	0.0140	12631	0.0969	1.603	14.279
45/55	351.1	1435	0.0167	15466	0.0455	1.668	16.392
50/50	339.7	1575	0.0249	21047	0.0420	1.790	17.275
52/48	333.7	1616	0.0259	19302	0.0435	1.809	20.464
55/45	324.2	1566	0.0346	20998	0.0408	1.856	20.963
60/40	311.0	1535	0.0396	22210	0.0329	1.894	22.139

Plots of $\log[(\varepsilon_m/\varepsilon)-1]$ vs. $\log(T-T_m)$ for x = 0.1 to 0.5 are shown in Fig 4.22, where linear relationships can be clearly seen. The γ and δ values of compositions in the system are represented in Fig 4.23. The parameter γ is determined from a slope of the plots to be between 1.60 and 1.89 and the diffusiveness parameter δ_γ is the intercept values ranging between 14.3 and 22.1 as shown in Table 4.6. All these extracted parameters also confirm that phase transition becomes more diffuse with increasing Zr content, as described earlier.

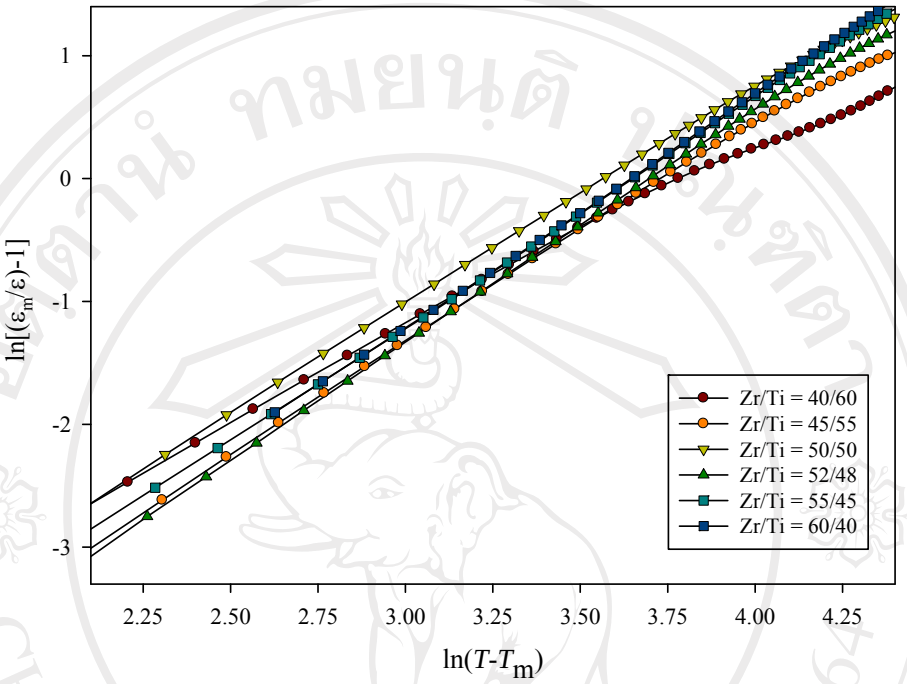

Figure 4.22 Dependence of log $[(\varepsilon_m/\varepsilon)-1]$ with $\log(T-T_m)$ for $0.2Pb(Zn_{1/3}Nb_{2/3})O_3$-$0.8Pb(Zr_xTi_{1-x})O_3$ ceramics.

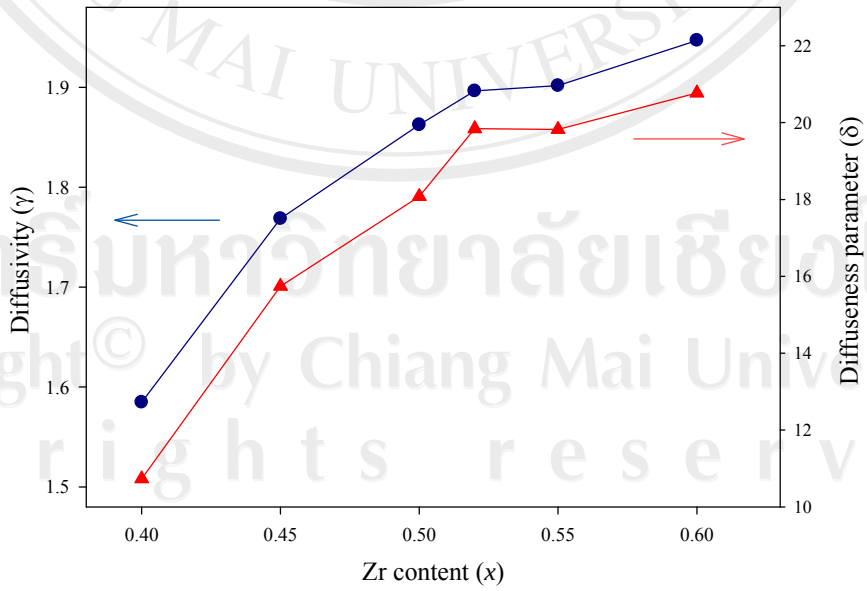

Figure 4.22 Dependence of diffusivity (γ) and diffuseness parameter (δ) for $0.2Pb(Zn_{1/3}Nb_{2/3})O_3$-$0.8Pb(Zr_xTi_{1-x})O_3$ ceramics.

4.3.2.3. Piezoelectric properties

Density, dielectric constant (ε_r), electromechanical coupling factor (k_p), mechanical quality factor (Q_m) and piezoelectric constant (d_{33}) are plotted as a function of the Zr content in Fig 4.24. The density is decreased with the increase of Zr contents approximately from 7.9 to 7.6 g/cm^3. When Zr content increases, the composition needs to be sintered at higher temperature [95]. Though, density is decreased, ε_r , k_p , d_{33} and Q_m are increased with the amount of Zr contents in the range of $0.40 \leq y \leq 0.50$, possibly indicating MPB of this system. However, ε_r , k_p , d_{33} and Q_m are decreased with the Zr content above 50 mole%. The variation of piezoelectric and dielectric properties shown in Table 4.7, clearly indicates the MPB of this system with optimized electrical properties. It is well known that the maximum *k* and *d* can be obtained around morphotropic phase boundary between the tetragonal and rhombohedral phase [96].

Table 4.7 Piezoelectric properties of $0.2Pb(Zn_{1/3}Nb_{2/3})O_3$-$0.8Pb(Zr_xTi_{1-x})O_3$ ceramics

Zr/Ti ratio	Piezoelectric properties			Ferroelectric properties (at 25 °C)						Strain % @ 4MV/m
	d_{33} (pC/N)	k_p	Q_m	P_r (C/m^2)	P_s (C/m^2)	E_C (MV/m)	P_r/P_s	E_c/E_{max}	Loop squareness (R_{sq})	
40/60	312	0.45	50	0.129	0.149	3.15	0.866	0.770	1.362	0.141
45/55	362	0.53	53	0.232	0.253	2.84	0.917	0.694	1.387	0.219
50/50	430	0.58	90	0.287	0.303	1.97	0.947	0.482	1.473	0.278
52/48	423	0.57	84	0.309	0.325	1.76	0.951	0.430	1.530	0.346
55/45	408	0.51	74	0.356	0.373	1.31	0.954	0.320	1.570	0.429
60/40	367	0.47	67	0.401	0.418	1.19	0.959	0.291	1.735	0.495

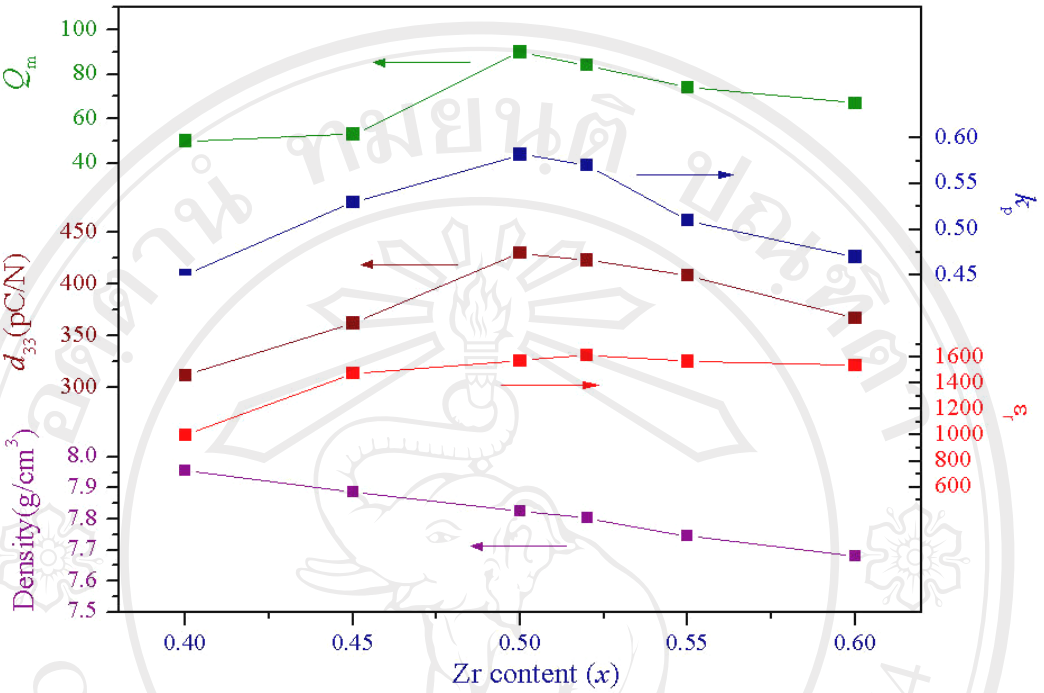

Figure 4.24 Density, dielectric constant (ε_r), piezoelectric constant (d_{33}), electromechanical coupling factor (k_p), and mechanical quality factor (Q_m) of $0.2Pb(Zn_{1/3}Nb_{2/3})O_3$- $0.8Pb(Zr_xTi_{1-x})O_3$ ceramics.

4.3.2.4. Ferroelectric properties

The polarization-field (P–E) hysteresis loops $0.2Pb(Zn_{1/3}Nb_{2/3})O_3$-$0.8Pb(Zr_xTi_{1-x})O_3$ ceramics are shown in Fig. 4.25. The well-developed and fairly symmetric hysteresis loops with the field are observed for all compositions. To further assess ferroelectric characteristics in Zr/Ti ratio on 0.2PZN-0.8PZT ceramics, the ferroelectric parameters, i.e. the remnant polarization (P_r) and the coercive field (E_c), have been extracted from the experimental data, as given in Table 4.7. However, since the ferroelectric properties of the ceramics depend strongly on both the poling and measuring fields, the ferroelectric parameters have been normalized in forms of P_r/P_s and E_c/E_{max} values, where P_s is the saturated polarization , E_{max} is maximum

applied field. These normalized values are listed in Table 4.7. It can be seen clearly that P_r/P_s increases with Zr content into the PZN–PZT composition and reachs the maximum values at Zr/Ti = 60/40 composition, where P_r achieves the level of 96% of the maximum polarization and E_c is as small as 29% of the maximum applied field. The ferroelectric characteristics can also be assessed with the hysteresis loop squareness (R_{sq}), which can be calculated from the empirical expression $R_{sq}=(P_r/P_s)+(P_{1.1Ec}/P_r)$, where P_r is the remnant polarization, P_s is the saturated polarization obtained at some finite field strength below the dielectric breakdown and $P_{1.1Ec}$ is the polarization at the field equal to $1.1E_c$ [93]. For the ideal square loop, R_{sq} is equal to 2.00. As listed in Table 4.7, the loop squareness parameter R_{sq} increases from 1.362 in Zr/Ti = 40/60 to reach the maximum value of 1.735 in Zr/Ti = 60/40.

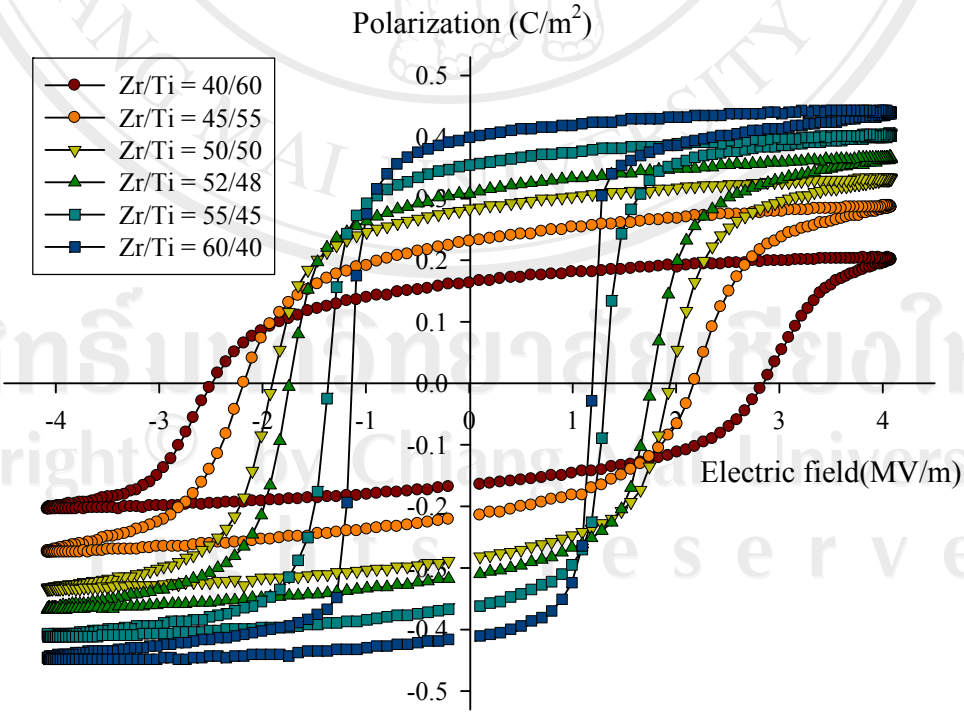

Figure 4.25 Polarization and electric filed of $0.2Pb(Zn_{1/3}Nb_{2/3})O_3$-$0.8Pb(Zr_xTi_{1-x})O_3$ ceramics.

The longitudinal strain (s) of the specimens as a function of the electric field is shown in Fig. 4.26. The strains are enhanced markedly when Zr content is increased. The strain level is strongly dependent on the Zr content since the Zr content controls rhombohedral domains in the system [94, 96]. When increased Zr content, the highest strain (0.495% at 4 MV/m) is observed in ceramic with Zr/Ti= 60/40, as listed in Table 4.7.

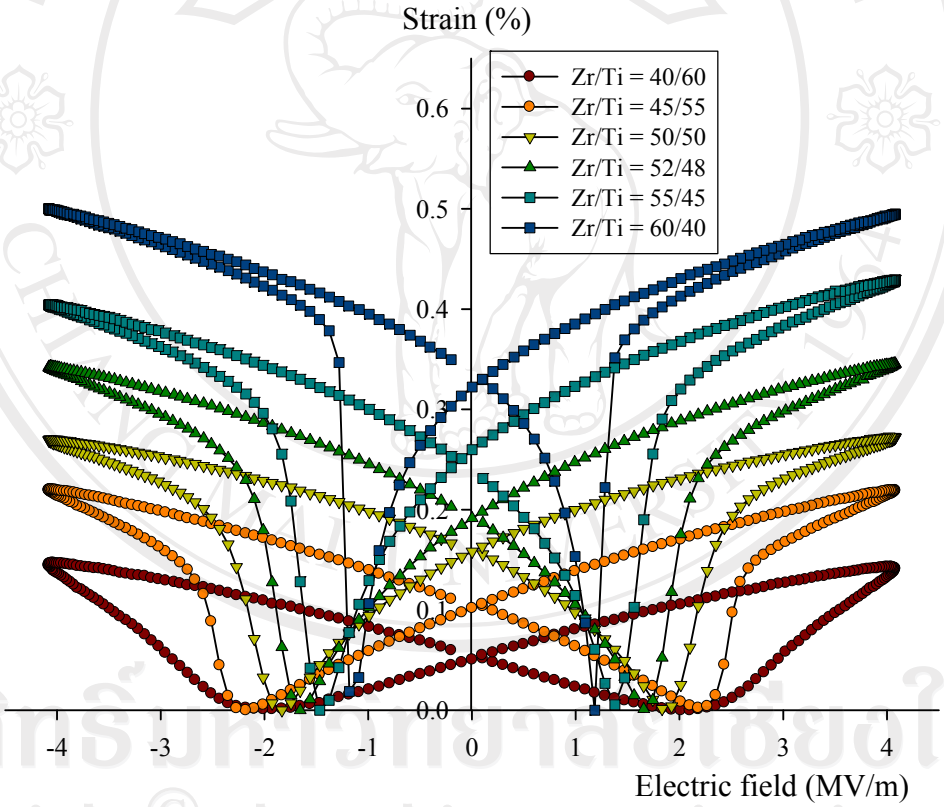

Figure 4.26 Strain and electric filed of $0.2Pb(Zn_{1/3}Nb_{2/3})O_3$-$0.8Pb(Zr_xTi_{1-x})O_3$ ceramics.

These results show ferroelectric and strain properties relationship with crystal structure. The tetragonal structure displays lower polarization, lower strain and higher E_c, as compared with the rhombohedral structure. This can be attributed to the

increase in tetragonal domains transformation into rhombohedral domains as the tetragonal structure in the PZT system decreases with the increase in Zr content [9, 96].

These results clearly show that Zr/Ti ratio can be used to optimize electrical properties of 0.2PZN-0.8PZT ceramics. The $0.2Pb(Zn_{1/3}Nb_{2/3})O_3$-$0.8Pb(Zr_{0.50}Ti_{0.50})O_3$ composition corresponds to the MPB, which is confirmed by the optimum electrical properties such as maximum of ε_r , k_p and d_{33}.

4.3.3. Summary

Ceramic composition $0.2Pb(Zn_{1/3}Nb_{2/3})O_3$-$0.8Pb(Zr_xTi_{1-x})O_3$, [0.2PZN–0.8PZT] solid solution system is expected to display excellent dielectric, piezoelectric, and ferroelectric properties as it is close to the morphotropic phase boundary (MPB) of PZN-PZT system. The electrical behavior of the ceramics with x= 0.40, 0.45, 0.50, 0.52, 0.55 and 0.60 has been characterized in order to identify the MPB compositions in this system. With combination of x-ray diffraction analysis, dielectric, piezoelectric and ferroelectric measurements, it was consistently shown that an MPB between tetragonal and rhombohedral phase exists around x = 0.50 -0.52 in this binary system. In addition, the transition temperature decreases with increasing Zr content in the system. The *P–E* and *s-E* loops demonstrate that PZN–PZT system changes gradually from tetragonal to rhombohedral phase with changing Zr/Ti ratio. These results clearly show the significance of Zr/Ti ratio in optimizing the electrical properties of the PZN–PZT system.